JOURNAL OF THERMOPHYSICS AND HEAT TRANSFER
Vol. 12, No. 3, July–September 1998

Finite Volume Method for Radiative Heat Transfer Using Unstructured Meshes

J. Y. Murthy* and S. R. Mathur†
Fluent Inc., Lebanon, New Hampshire 03766

The finite volume method has been shown to accurately predict radiative heat transfer in absorbing, emitting, and scattering media. However, computations have for the most part been restricted to structured, body-fitted meshes. In this paper a conservative cell-based numerical scheme is devised for computing radiative heat transfer using meshes composed of arbitrary unstructured polyhedra. The method is shown to be robust and accurate through comparisons with published solutions.

Nomenclature

$\boldsymbol{A}$ = area vector
C_p = specific heat at constant pressure
Gr = Grashof number
I = intensity
I_b = blackbody intensity
k = conductivity
Nu = Nusselt number
N_θ, N_ϕ = polar and azimuthal discretization
Pl = Planck number
Pr = Prandtl number
q = heat flux
Ra = Rayleigh number
$\boldsymbol{r}$ = position vector
s = coordinate along ray
$\boldsymbol{s}$ = ray direction vector
T = temperature
u_j = velocity in coordinate direction j
x_j = coordinate direction
ΔV = volume of control volume
θ = polar angle
κ = absorption coefficient
ν = kinematic viscosity
ρ = density
σ = Stefan–Boltzmann constant
σ_s = scattering coefficient
Φ = scattering phase function
ϕ = azimuthal angle
Ω = solid angle

Introduction

THERE has been considerable research in the use of unstructured meshes for the computation of fluid flow and heat transfer during the last decade.[1–3] Unstructured meshes greatly simplify the mesh generation task and enable the routine use of computational fluid dynamics in practical industrial applications. Unstructured mesh methods are now available for solving compressible and incompressible industrial flows in the presence of turbulence, rotation, swirl, combustion, and other complexities. Many of these industrial applications require the computation of radiation in absorbing, emitting, and scattering media. It is desirable to devise schemes for radiation heat transfer that are consistent with the unstructured mesh solvers used for fluid flow, so that a single unified spatial discretization is used throughout.

A variety of methods for computing radiative heat transfer in absorbing, emitting, and scattering media have appeared in the literature.[4] Among the most widely used are zonal methods,[5] Monte Carlo methods,[5] the class of P_N approximations,[6] ray-tracing methods such as the discrete transfer model,[7] and the discrete-ordinates method.[8] More recently, Chui and Raithby[9,10] developed the finite volume scheme for radiative heat transfer by imposing energy conservation principles over discrete solid angles. A similar approach has been taken by Chai and co-workers.[11,12] Early work was restricted to either Cartesian or cylindrical meshes. Chui and Raithby[10] extended the finite volume scheme to nonorthogonal body-fitted meshes. Chai et al.[11] developed a cell-based finite volume method using structured body-fitted meshes. Fiveland and Jessee[8] developed an even-parity form of the discrete-ordinates formulation using a finite element method. Though some of these methods[8,10,11] are, in principle, capable of addressing unstructured meshes, no systematic application and evaluation of these methods has been done in the unstructured mesh context.

The objective of this paper is to develop a finite volume method for participating radiation within the unstructured-mesh framework outlined by Mathur and Murthy.[1] Unlike the node-based schemes used by Chui and Raithby and Fiveland and Jessee, a cell-centered formulation based on arbitrary polyhedral control volumes is developed. The radiative transfer equation (RTE) is solved for a discrete number of finite solid angles. For each direction the RTE is integrated over the control volume and discretized using ideas similar to those for fluid flow. An algebraic multigrid method is used for the solution of linear equations. Special attention is paid to the treatment of control-angle overhang not only at boundaries but also at the interior. Though the present work is restricted to a gray gas with diffuse-gray boundaries, the basic methodology can be extended to nongray radiation and other types of boundary conditions. The method is validated against analytical and numerical solutions in the literature and shown to perform satisfactorily.

Governing Equations

The radiative transfer equation for a gray absorbing, emitting, and scattering gas in the direction $\boldsymbol{s}$ may be written as[5]

$$\frac{\mathrm{d}I}{\mathrm{d}s} = -[\kappa(\boldsymbol{r}) + \sigma_s(\boldsymbol{r})]I(\boldsymbol{r}, \boldsymbol{s}) + S(\boldsymbol{r}, \boldsymbol{s}) \tag{1}$$

Received Oct. 13, 1997; revision received Jan. 9, 1998; presented as Paper 98-0860 at the AIAA 36th Aerospace Sciences Meeting, Reno, NV, Jan. 12–15, 1998; accepted for publication Feb. 16, 1998.

*Technical Lead, 10 Cavendish Court. Member AIAA.
†New Business Development, 10 Cavendish Court. Member AIAA.

where

$$S = \kappa(\boldsymbol{r})I_b(\boldsymbol{r}) + \frac{\sigma_s(\boldsymbol{r})}{4\pi}\int_{4\pi} I(\boldsymbol{r}, \boldsymbol{s}')\Phi(\boldsymbol{s}', \boldsymbol{s})\, d\Omega' \qquad (2)$$

Because $\boldsymbol{s}$ is constant, Eq. (1) may be written as

$$\frac{\partial Is_i}{\partial x_i} = -[\kappa(\boldsymbol{r}) + \sigma_s(\boldsymbol{r})]I(\boldsymbol{r}, \boldsymbol{s}) + S(\boldsymbol{r}, \boldsymbol{s}) \qquad (3)$$

where s_i are the components of $\boldsymbol{s}$.

Boundary Conditions

All boundaries are assumed to be gray-diffuse. Under this assumption, the boundary intensity I_w for all outgoing directions ($\boldsymbol{s}\cdot\boldsymbol{n} < 0$) is given by

$$I_w = \frac{(1-\varepsilon)}{\pi}\int_{\boldsymbol{s}\cdot\boldsymbol{n}>0} I(\boldsymbol{s})\boldsymbol{s}\cdot\boldsymbol{n}\, d\Omega + \frac{\varepsilon\sigma T_w^4}{\pi} \qquad (4)$$

Here, T_w is the boundary temperature and ε is its emissivity. The unit vector $\boldsymbol{n}$ is the surface normal pointing out of the domain.

Energy Equation

For problems in which radiative equilibrium does not exist, it is necessary to solve the energy equation. For the steady constant property flow of an incompressible fluid, the energy equation may be written as

$$\frac{\partial \rho u_j C_p T}{\partial x_j} = \frac{\partial}{\partial x_j}\left(k\frac{\partial T}{\partial x_j}\right) + S_h \qquad (5)$$

Here S_h contains the source of energy. The radiative contribution to S_h for a gray absorbing, emitting, and scattering gas may be written as

$$\kappa(\boldsymbol{r})\int_{4\pi}[I(\boldsymbol{r}, s) - I_b(\boldsymbol{r})]\, d\Omega \qquad (6)$$

Numerical Method

Spatial Discretization

The domain is discretized into arbitrary unstructured convex polyhedra called *cells*. The boundaries surrounding the cells are called *faces* and the vertices of the polyhedra are referred to as *nodes*. Each internal face has two cells on either side. Line segments joining the nodes are termed *edges* (and are identical to faces in two dimensions). Because the algorithm is applicable to arbitrary polyhedra, nonconformal interfaces such as those shown in Fig. 1 require no special treatment, unlike other approaches.[12] The cell $C0$ is simply treated as a polyhedron with faces a-b-c-d. All unknowns are stored at cell centers.

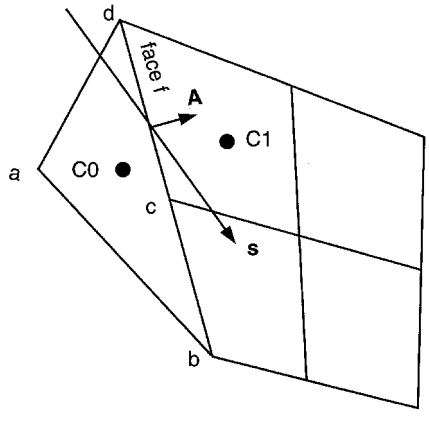

Fig. 1 Control volume.

Angular Discretization

The angular space 4π at any spatial location is discretized into discrete nonoverlapping solid angles ω_i, the centroids of which are denoted by the direction vector $\boldsymbol{s}_i$. Though the discretization of angular space can in principle be unstructured, here we adopt a structured discretization, with each octant being discretized into $N_\theta \times N_\phi$ solid angles. The angles θ and ϕ are the polar and azimuthal angles, respectively, and are measured with respect to the global Cartesian system (x, y, z); θ is measured from the z axis and ϕ is measured from the y axis. The angular discretization is uniform in that the polar direction is divided into N_θ equal angles, and the azimuthal direction is divided into N_ϕ equal angles. The subtended solid angles, however, are not equal, and vary with θ. The quantities (θ_i, ϕ_i) denote the polar and azimuthal angles associated with the centroid of the solid angle ω_i; the extents are given by $\Delta\theta$ and $\Delta\phi$.

Control Volume Balance

For each discrete direction i Eq. (3) is integrated over the the control volume $C0$ in Fig. 1 and the solid angle ω_i to yield

$$\sum_f J_f I_{if} = [-(\kappa + \sigma_s)I_{i0} + S_i]\omega_i \Delta V_0 \qquad (7)$$

Here, I_{if} is the intensity associated with the direction i at the face of the control volume, and I_{i0} is the intensity at the cell $C0$ in the direction i. J_f is a geometric factor defined next. ΔV_0 is the volume of the control volume $C0$. The solid angle ω_i is given by

$$\omega_i = \int_{\Delta\phi}\int_{\Delta\theta} \sin\theta\, d\theta\, d\phi = 2\sin\theta_i \sin\left(\frac{\Delta\theta}{2}\right)\Delta\phi \qquad (8)$$

Because the integration is exact, $\Sigma_i \omega_i = 4\pi$ is identically satisfied.

The source term S_i is given by

$$S_i = \kappa I_{b0} + \frac{\sigma_s}{4\pi}\sum_j I_{j0}\gamma_{ij} \qquad (9)$$

where

$$\gamma_{ij} = \frac{1}{\omega_i}\int_{\omega_i}\int_{\omega_j} \Phi(\boldsymbol{s}_{i'}\cdot\boldsymbol{s}_{j'})\, d\omega_{j'}\, d\omega_{i'} \qquad (10)$$

The blackbody intensity I_{b0} is based on the temperature of the cell $C0$ and I_{j0} are the cell intensities in the directions j. The treatment of the left-hand side of Eq. (7) is addressed next.

For body-fitted and unstructured meshes, the discretization of the left-hand side (LHS) of Eq. (7) is complicated by the possibility of control-angle overhangs. Because the directions $\boldsymbol{s}_i$ are defined with respect to a global coordinate system (x, y, z), the boundaries of the discrete solid angles ω_i do not necessarily align with control volume faces. Mathematically, an overhanging control angle is one for which $(\boldsymbol{s}_{ji}\cdot\boldsymbol{A},\ j = 1, 4)$ are not all of the same sign. Here, $\boldsymbol{s}_{ji}$ is the ray vector to the jth corner of the ith control angle. This is illustrated in two dimensions in Fig. 2. In three dimensions, the intersection of the control-volume face with the angular discretization is more complex. The line of intersection between the control volume face and the sphere is a great circle; the arbitrary intersections between the discrete solid angle and this great circle determine the amount of overhang. This problem does not occur in Cartesian meshes. It may also be avoided in structured body-fitted meshes by using local coordinates. For unstructured meshes,

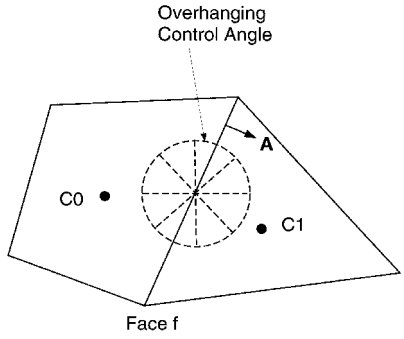

Fig. 2 Control angle overhang in two dimensions.

however, no such local coordinate can be defined and special procedures must be adopted.

Face Intensity Treatment

For directions i with no control angle overhang at the face f, the following treatment is used. The LHS of Eq. (7) is written as

$$J_f I_{if} = I_{if}\boldsymbol{A} \cdot \int_{\Delta\theta}\int_{\Delta\phi} \boldsymbol{s} \sin\theta \, d\theta \, d\phi \tag{11}$$

Here

$$\boldsymbol{s} = \sin\theta \sin\phi \boldsymbol{i} + \sin\theta \cos\phi \boldsymbol{j} + \cos\theta \boldsymbol{k} \tag{12}$$

Computing the integral in Eq. (11) we get

$$J_f I_{if} = I_{if}\boldsymbol{A} \cdot S_i \tag{13}$$

where

$$\begin{aligned} S_i = {} & \sin\phi_i \sin(0.5\Delta\phi)(\Delta\theta - \cos 2\theta_i \sin\Delta\theta)\boldsymbol{i} \\ & + \cos\phi_i \sin(0.5\Delta\phi)(\Delta\theta - \cos 2\theta_i \sin\Delta\theta)\boldsymbol{j} \\ & + 0.5\Delta\phi \sin 2\theta_i \sin\Delta\theta \boldsymbol{k} \end{aligned} \tag{14}$$

Thus, the angular integration in Eq. (11) is exact. The vector $\boldsymbol{A}$ is the outward-pointing area vector with respect to cell $C0$, as shown in Fig. 1.

Using a step approximation for I_{if} we may write

$$I_{if} = I_{i,\text{upwind}} \tag{15}$$

Here $I_{i,\text{upwind}}$ is the value of I_i in the "upwind" cell.

Treatment of Control-Angle Overhang

Two different approaches have been proposed in the literature to address control-angle overhang. Chui and Raithby[10] proposed a treatment for control-angle overhang at boundaries for two dimensions but do not address it at interior faces. Their treatment requires the definition of neighbor directions that are fully incoming or fully outgoing. This is workable in two dimensions, but such directions cannot uniquely be identified for general three-dimensional overhangs. Chai et al.[11] treated control-angle overhang by assuming that the entire control angle is either incoming or outgoing at a face depending on whether the mean direction $\boldsymbol{s}_i$ is incoming or outgoing. The latter treatment is inexpensive and conceptually simple. Chai et al.[11] and others have reported reasonable agreement with analytical results for coarse spatial and angular discretizations. However, no systematic assessment of the applicability of this treatment has been made because of the difficulty in treating general three-dimensional overhangs.

Here two approaches are explored: The first (A) is the approach of Chai et al.[11] and the second (B) is a treatment of three-dimensional overhang; each is described in turn.

Approach A

In this approach, at each face of the cell $C0$, the solid angle associated with the direction i is assumed to be outgoing to the cell if $\boldsymbol{s}_i \cdot \boldsymbol{A} > 0$ and incoming otherwise. The treatment of I_{if} in either event is identical to the treatment for nonoverhanging directions. Using the step scheme, the cell intensity at the appropriate upwind cell is used for I_{if}.

Approach B (Pixelation)

If the direction i exhibits overhang at the face f, the incoming and outgoing portions of the solid angle are differenced differently. Equation (11) is written as

$$J_f I_{if} = I_{if,\text{out}}\alpha_{i,\text{out}} + I_{if,\text{in}}\alpha_{i,\text{in}} \tag{16}$$

where

$$\alpha_{i,\text{out}} = \boldsymbol{A} \cdot \int_{\Delta\theta}\int_{\Delta\phi} \boldsymbol{s} \sin\theta \, d\theta \, d\phi, \qquad \boldsymbol{s}\cdot\boldsymbol{A} > 0 \tag{17}$$

$$\alpha_{i,\text{in}} = \boldsymbol{A} \cdot \int_{\Delta\theta}\int_{\Delta\phi} \boldsymbol{s} \sin\theta \, d\theta \, d\phi, \qquad \boldsymbol{s}\cdot\boldsymbol{A} \le 0 \tag{18}$$

The incoming and outgoing face intensities are then written as in Eq. (15). Thus, referring to Fig. 1, we may write

$$J_f I_{if} = I_{i0}\alpha_{i,\text{out}} + I_{i1}\alpha_{i,\text{in}} \tag{19}$$

where I_{i0} and I_{i1} refer to the intensities in cells $C0$ and $C1$, respectively, in the direction i, and the terms *incoming* and *outgoing* are with respect to $C0$.

Overhang Angle Computation

The computation of the overhang angles may be accomplished in a number of ways. In the present work, the solid angle of interest is divided into $N_{\theta_p} \times N_{\phi_p}$ pixels. Each pixel is identified by a pixel direction $\boldsymbol{s}_{\text{pi}}$ written in terms of the pixel centroid angles (θ_{pi}, ϕ_{pi}) as

$$\boldsymbol{s}_{\text{pi}} = \sin\theta_{\text{pi}} \sin\phi_{\text{pi}} \boldsymbol{i} + \sin\theta_{\text{pi}} \cos\phi_{\text{pi}} \boldsymbol{j} + \cos\theta_{\text{pi}} \boldsymbol{k} \tag{20}$$

We may then write Eqs. (17) and (18) as

$$\alpha_{i,\text{out}} = \boldsymbol{A} \cdot \sum_{\boldsymbol{s}_{\text{pi}}\cdot\boldsymbol{A}>0} S_{\text{pi}} \tag{21}$$

$$\alpha_{i,\text{in}} = \boldsymbol{A} \cdot \sum_{\boldsymbol{s}_{\text{pi}}\cdot\boldsymbol{A}\le 0} S_{\text{pi}} \tag{22}$$

where S_{pi} is written analogously to Eq. (14), using the pixel angles (θ_{pi}, ϕ_{pi}) rather than (θ_i, ϕ_i). The summation is over all pixels in the control angle.

Using this approach, control angle overhang can be computed up to the pixel resolution. Computational effort may be minimized by only pixelating those control angles that exhibit overhang.

Boundary Conditions

The following steps are usually required at gray-diffuse boundaries: 1) Computation of the incoming radiation, 2) update of boundary intensity, and 3) computation of incoming and/or outgoing radiation flux in each of the angular directions i for inclusion in the individual transport equation.

The radiation incoming to the boundary is computed from

$$q^- = \int_{4\pi} I\boldsymbol{s}\cdot\boldsymbol{A}\ \mathrm{d}\Omega, \qquad \boldsymbol{s}\cdot\boldsymbol{A} > 0 \tag{23}$$

where $\boldsymbol{A}$ is the surface area vector pointing out of the domain.

As with interior faces, special considerations because of control angle overhang also apply at boundaries. Here, incoming and outgoing intensities in any direction i may be substantially different from each other, and it may be argued that the incoming and outgoing portions of the solid angle should be treated differently. Again, we consider the two different approaches outlined earlier.

Approach A

Here, the incoming radiation is written as

$$q^- = \boldsymbol{A}\cdot\sum_i I_{i0}\boldsymbol{S}_i \quad \text{for} \quad \boldsymbol{s}_i\cdot\boldsymbol{A} > 0 \tag{24}$$

Thus, a solid angle is considered incoming to the boundary if its mean direction $\boldsymbol{s}_i$ is incoming. The boundary intensity I_w is updated using Eq. (4). The boundary radiation transfer for each of the directions i is written as

$$J_f I_{if} = \begin{cases} I_{i0}\boldsymbol{A}\cdot\boldsymbol{S}_i & \text{if} \quad \boldsymbol{s}_i\cdot\boldsymbol{A} > 0 \\ I_w\boldsymbol{A}\cdot\boldsymbol{S}_i & \text{if} \quad \boldsymbol{s}_i\cdot\boldsymbol{A} \le 0 \end{cases} \tag{25}$$

Approach B (Pixelation)

Here, the incoming radiation is written as

$$q^- = \sum_i I_{i0}\alpha_{i,\mathrm{in}} \tag{26}$$

where I_{i0} is the value of I_i in the near-boundary cell $C0$, $\alpha_{i,\mathrm{in}}$ is the integral defined in Eq. (18) and is incoming to the boundary, and $\boldsymbol{A}$ is the boundary face area vector pointing out of the domain. Thus, only those parts of the overhang solid angle that are incoming are included in the incoming radiative flux. Once q^- is available, the boundary intensity I_w is updated using Eq. (4).

The boundary radiative transfer for each of the directions i is written as

$$J_f I_{if} = I_{i0}\alpha_{i,\mathrm{in}} + I_w\alpha_{i,\mathrm{out}} \tag{27}$$

Here, the incoming and outgoing directions are defined with respect to the boundary, not the cell $C0$. The quantities $\alpha_{i,\mathrm{in}}$ and $\alpha_{i,\mathrm{out}}$ are computed as for interior faces, using pixelation. For directions with no overhang, either $\alpha_{i,\mathrm{in}}$ or $\alpha_{i,\mathrm{out}}$ is zero.

Linear Solver

The discretization procedure leads to a set of (nominally) linear equations relating the value of I_i at the cell center to its cell neighbors:

$$a_p I_{i\mathrm{p}} = \sum_{\mathrm{nb}} a_{\mathrm{nb}} I_{i\mathrm{nb}} + b \tag{28}$$

Here, nb is the number of cell neighbors. The intensities associated with other discrete directions are included in the b term. The algebraic set for each i is solved iteratively, looping through all of the discrete directions in turn until convergence.

In solving Eq. (28), no attempt is made to order cells in the upwind direction. Instead, the system is solved using an algebraic multigrid procedure[13] that constructs coarse level equations by clustering a fine level cell with the neighbor for which the influence coefficient is the highest. This, in effect, ensures efficient transport of information along the ray direction. For the examples in this paper, the Brandt cycle is used for intensity calculations. A Gauss–Seidel relaxation procedure is used at each multigrid level.

Coupling with Energy Equation

Procedures for the discretization of the energy equation are similar to those for scalar transport described in Mathur and Murthy[1] and are not described further. Equation (6) is written as

$$S_h = S_h^* + \left.\frac{\partial S_h}{\partial T}\right|_{T^*}(T - T^*) \tag{29}$$

Here T^* is the current iterate of the temperature of the participating medium. Using $I_b = \sigma T^4/\pi$ in Eq. (6), the source term in the discrete energy equation is written as

$$S_h\Delta V_0 = \Delta V_0\left(\kappa\sum_i \omega_i I_{i0} - 4\kappa\sigma T^4\right) \tag{30}$$

Assuming I_{i0} independent of T and evaluating $\partial S_h/\partial T$ from the second term in Eq. (30), we may write

$$S_h\Delta V_0 = \Delta V_0\left(\kappa\sum_i \omega_i I_{i0} + 12\kappa\sigma T^{*4} - 16\kappa\sigma T^{*3}T\right) \tag{31}$$

The last term in Eq. (31) is included implicitly in the discrete energy equation; the other terms are included explicitly. Similar procedures are employed at boundaries. The energy and intensity equations are iterated sequentially until convergence.

Results

Here we present results for a variety of participating radiation problems. In the following sections $N_\theta \times N_\phi$ refers to the angular discretization of the octant. Unless otherwise stated, all results using pixelation (approach B) are obtained with $N_{\theta_p} \times N_{\phi_p}$ of 1×10 in two-dimensional cases and 10×10 in three-dimensional cases. The error reported next is defined as

$$\frac{1}{N}\sum_n \frac{|f_n - f_{n,\mathrm{exact}}|}{|f_{n,\mathrm{exact}}|} \tag{32}$$

where f_n is the computed value at point n, $f_{n,\mathrm{exact}}$ is the exact value at the same point, and N is the total number of points.

Radiation in Quadrilateral Enclosure with Isothermal Medium

We consider here the case of participating radiation in a quadrilateral box containing an absorbing and emitting medium at $T = T_h$. The vertices of the box, in counterclockwise order, are (0,0), (2.2, 0), (1.5, 1.2), and (0.5, 1.0). All dimensions are in meters. The walls are numbered counterclockwise, with wall 1 joining and (0, 0) and (2.2, 0), and are at $T = 0$. The objective is to predict the dimensionless incoming radiative flux $q^* = q/(\sigma T_h^4)$ on the lateral walls and to compare it with the exact solution, generated by means of a ray-tracing method. This problem has been used by Chai et al.[11] to validate their finite volume scheme.

An initial structured mesh of 10×10 quadrilateral control volumes is used, with an $N_\theta \times N_\phi$ of 1×2; approach A (no pixelation) is used. This discretization is identical to that used by Chai et al.[11] The numerical scheme also defaults identically to theirs when the step scheme is used on a structured quadrilateral mesh. Plots of q^* vs the length along wall 1 for various values of absorption coefficient κ are shown in Fig. 3. The agreement with the exact solution is within 4%. Figure 4 shows the variation of q^* along walls 2, 3, and 4 for $\kappa = 1.0$ m^{-1}. Here s, the length along the wall, is measured counterclockwise. The departures from the exact solution are espe-

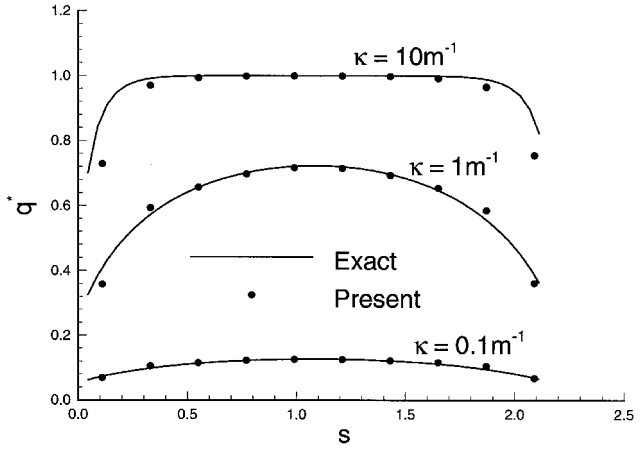

Fig. 3 Quadrilateral enclosure with isothermal medium, heat flux on wall 1.

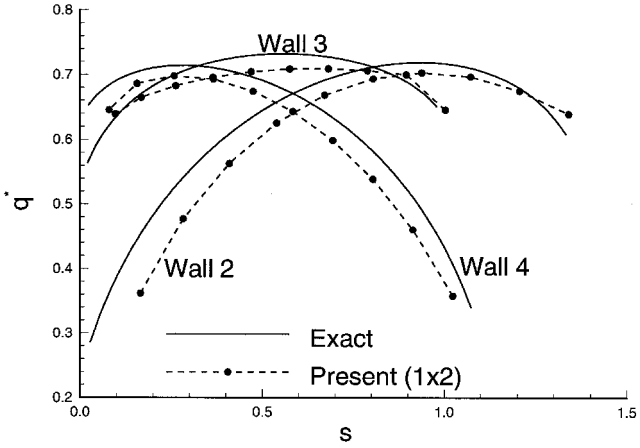

Fig. 4 Quadrilateral enclosure with isothermal medium, heat flux on walls 2, 3, and 4 for $\kappa = 1.0\ m^{-1}$.

cially high at the corners for walls 2 and 4. The errors for these cases are tabulated in Table 1.

Results from a finer structured quadrilateral mesh of 40 × 40 cells are shown in Fig. 5 for wall 3 for $\kappa = 1.0\ m^{-1}$. A variety of angular discretizations are used. The errors for all computations using the 40 × 40 mesh are shown in Table 1. For coarse angular discretizations (2 × 2) the influence of the corners is not captured well by the computation. For finer angular discretizations, the computed solutions match the exact solution well. Small departures are still seen at the corners of the domain, where even finer angular resolution is probably required. To quantify the influence of control angle overhang, computations were done using approach B (pixelation) at boundaries, but not at interior faces. For coarse angular discretizations, boundary pixelation does not improve the answer very much. For very fine angular discretizations (2 × 8), the results with and without pixelation are nearly identical, as expected. Pixelation appears to make a difference in the intermediate range (2 × 4).

To study the effect of pixelation, the degree of boundary pixelation was varied. The 40 × 40 mesh was used, with $\kappa = 1.0\ m^{-1}$ and a 2 × 4 angular discretization. Pixelations of 1 × 4 and 1 × 10 were used and compared to the case with no pixelation. The 1 × 4 and 1 × 10 pixelation are virtually identical. Interior pixelation was found to not make any difference to the solution.

For complex geometries a certain minimum angular discretization is required to resolve significant geometric features. To resolve features of length δ, a solid angle resolution of $\mathcal{O}(\delta^2/R^2)$ is required at a surface at a distance R from the feature. Pixelation cannot improve accuracy unless this basic angular resolution is met. On the other hand, when the angular resolution is very fine, the solid angles associated with overhanging control angles are small, and their influence is consequently small. For many practical problems, it appears that approach A will suffice.

Figure 6 shows an unstructured triangular mesh of 2600 cells. Radiative flux on wall 3 is shown for this mesh in Fig. 7 for $\kappa = 1.0\ m^{-1}$. Again, results with and without boundary pixelation are shown. The results are very similar to those for

Table 1 Quadrilateral enclosure with isothermal medium[a]

Case	Error, %
10 × 10 mesh, $N_\theta \times N_\phi = 1 \times 2$, approach A:	
Wall 1	
$\kappa = 0.1\ m^{-1}$	3.06
$\kappa = 1.0\ m^{-1}$	3.15
$\kappa = 10.0\ m^{-1}$	3.64
Wall 2	
$\kappa = 1.0\ m^{-1}$	6.13
Wall 3	
$\kappa = 1.0\ m^{-1}$	2.15
Wall 4	
$\kappa = 1.0\ m^{-1}$	5.52
40 × 40 mesh, wall 3, $\kappa = 1.0\ m^{-1}$, approach A:	
$N_\theta \times N_\phi = 2 \times 2$	2.94
$N_\theta \times N_\phi = 2 \times 4$	1.12
$N_\theta \times N_\phi = 2 \times 8$	0.36
$N_{\theta_p} \times N_{\phi_p} = 1 \times 10$, approach B:	
$N_\theta \times N_\phi = 2 \times 2$	2.59
$N_\theta \times N_\phi = 2 \times 4$	0.69
$N_\theta \times N_\phi = 2 \times 8$	0.34
40 × 40 mesh, wall 3, $\kappa = 1.0\ m^{-1}$, $N_\theta \times N_\phi = 2 \times 4$, approach B (pixelation):	
$N_{\theta_p} \times N_{\phi_p} = 1 \times 4$	0.69
$N_{\theta_p} \times N_{\phi_p} = 1 \times 10$	0.69

[a]Error in q^* for quadrilateral mesh.

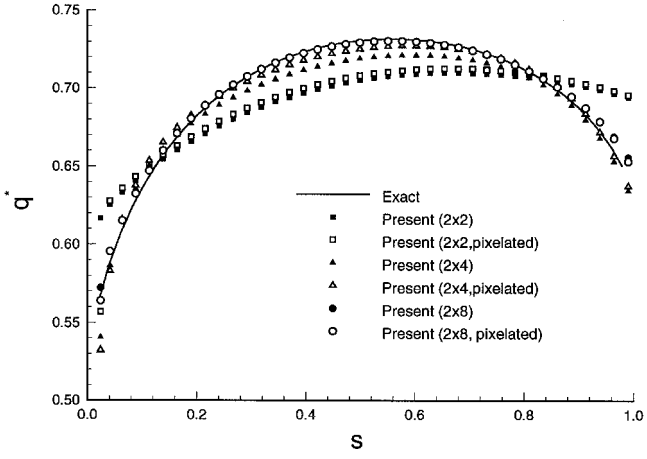

Fig. 5 Quadrilateral enclosure with isothermal medium, heat flux on wall 3 for 40 × 40 quadrilateral mesh for $\kappa = 1.0\ m^{-1}$.

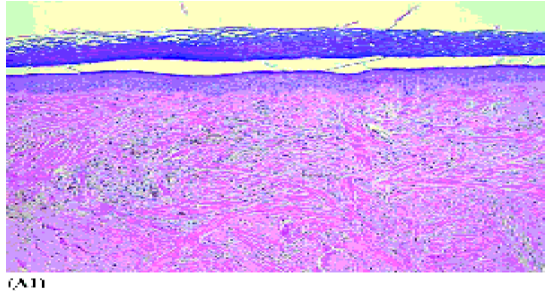

Fig. 6 Quadrilateral enclosure with isothermal medium, unstructured triangular mesh.

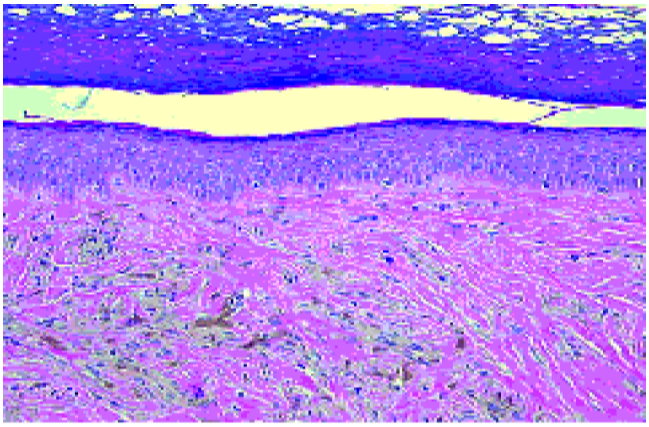

Fig. 7 Quadrilateral enclosure with isothermal medium, heat flux on wall 3 for triangular mesh for $\kappa = 1.0\ m^{-1}$.

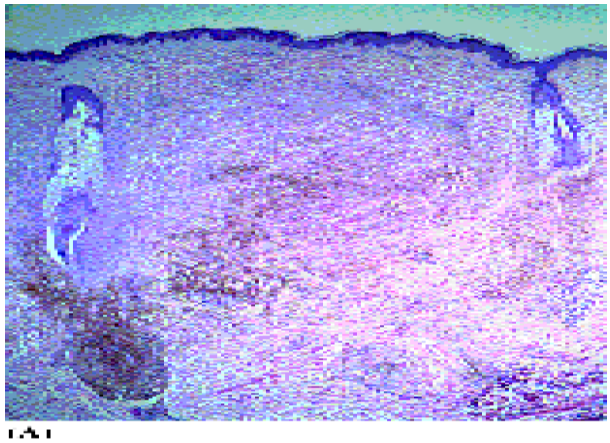

Fig. 8 Quadrilateral enclosure with non-isothermal medium, heat flux on wall 3 for global pixelation.

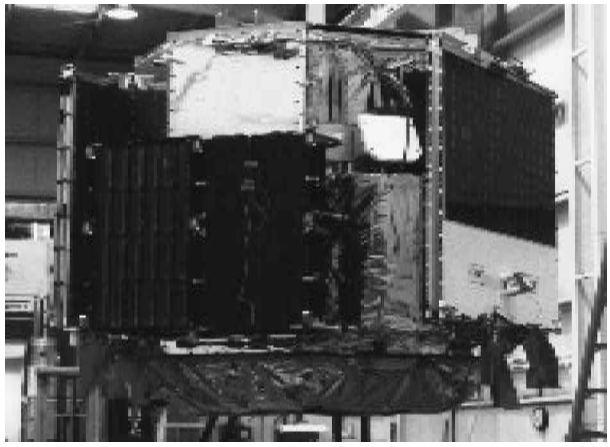

Fig. 9 Quadrilateral enclosure with non-isothermal medium, heat flux on wall 3 for $N_\theta \times N_\phi = 4 \times 4$.

the structured quadrilateral mesh. The errors for the unpixelated 2×2, 2×4, and 2×8 angular discretizations are 2.93, 0.81, and 0.58%, respectively. For the 2×2, 2×4, and 2×8 cases with boundary pixelation, the errors are 2.23, 0.59, and 0.50%, respectively.

All computations were done using a Sun Ultra 1 workstation. The computer code assumed an unstructured data structure even when a structured mesh was used. For the 40×40 quadrilateral mesh using approach A, the 2×2, 2×4, and 2×8 angular discretizations took 3.53, 6.58, and 12.77 s, respectively. For approach B, the 1×4 pixelation required 0.6% more computational time than the case with no pixelation; the 1×10 pixelation required 1.37% more. Thus, the resources required for boundary pixelation are very modest in two-dimensional geometries.

For the 2600 cell triangular mesh with approach A, the timings for the 2×2, 2×4, and 2×8 angular discretizations were 5.59, 10.67, and 21.24 s, respectively. The triangular mesh has 3982 faces. The 40×40 quadrilateral mesh has 3280 faces. The cost of equation discretization is approximately proportional to the number of faces in the mesh. The cost of the linear multigrid solution is proportional to the number of cells. The measured solution time scales as the number of cells, suggesting that the linear equation solver accounts for the greatest proportion of the time taken. Thus, quadrilateral and triangular meshes with the same number of cells are expected to show roughly similar performance even though the former has approximately two faces per cell and the latter has approximately 1.5.

Radiation in Quadrilateral Enclosure with Nonisothermal Medium

This problem is the same as the previous problem, except that the temperature of the enclosed medium is allowed to vary linearly as

$$T = T_A + [(T_B - T_A)/L](x^2 + y^2)^{1/2}\ (\mathrm{K}) \qquad (33)$$

The calculations are done for $T_A = 1000$ K, $T_B = 2000$ K, and $L = 1.921$ m. The dimensionless incoming radiative flux $q^* = q/(\sigma T_A^4)$ on wall 3 is compared to the exact solution, generated by a ray-tracing scheme. Computations are done using the 40×40 quadrilateral mesh, with approach A, approach B with only boundary pixelation, and approach B with both boundary and interior pixelation (referred to as global pixelation). The objective is to examine whether temperature variations, encountered in real-life radiation problems, require pixelation.

Figure 8 shows the variation of q^* along wall 3 for the case of global pixelation. For coarse angular discretizations (2×2), there is substantial departure, of the order of 10%, from the exact solution, at the right-hand corner. The error decreases as the angular discretization is made finer. Figure 9 compares calculations with approach A, approach B with boundary pixelation, and approach B with global pixelation for a 4×4 angular discretization. Though pixelation helps somewhat, the pixelated and unpixelated cases give similar results. For approach A, the error levels for angular discretizations of 2×2, 4×4, and 8×8 were 3.89, 2.24, and 1.12%, respectively. For approach B with only boundary pixelation, the corresponding error levels were 3.34, 1.61, and 1.07%, respectively. For approach B with global pixelation, the error levels were 3.05, 1.47, and 1.07%, respectively. It appears that approach A will yield satisfactory solutions even in the presence of a nonisothermal medium, as long as a certain basic angular discretization capable of resolving the gross geometry and temperature variations is employed.

Radiation in Tetrahedral Enclosure

To demonstrate the use of the scheme for three-dimensional geometries, we compute radiative heat transfer in a tetrahedron of side L. The base of the tetrahedron lies on the x–y plane; the coordinates (x/L, y/L, z/L) of the vertices are (0, 0, 0), (1, 0, 0), (0.5, 0.866, 0), and (0.5, 0.288, 0.817). The walls are at $T = 0$. The interior has a fixed temperature of $T = T_h$ and an optical thickness $\kappa L = 1.0$.

Two different tetrahedral meshes, of 1054 and 10,934 cells, are used; the coarse mesh is shown in Fig. 10. The dimensionless incoming heat flux q^* [$=q/(\sigma T_h^4)$] is computed along the line joining the side midpoint (0.75, 0.433, 0) and the vertex (0.5, 0.288, 0.817) for different angular discretizations, with and without boundary pixelation. The results for the

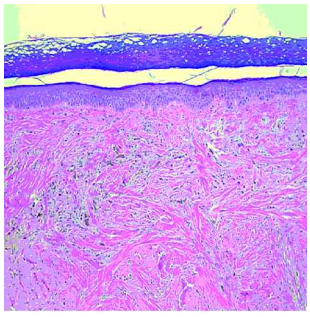

(A1)

Fig. 10 Tetrahedral enclosure, coarse mesh of 1054 cells.

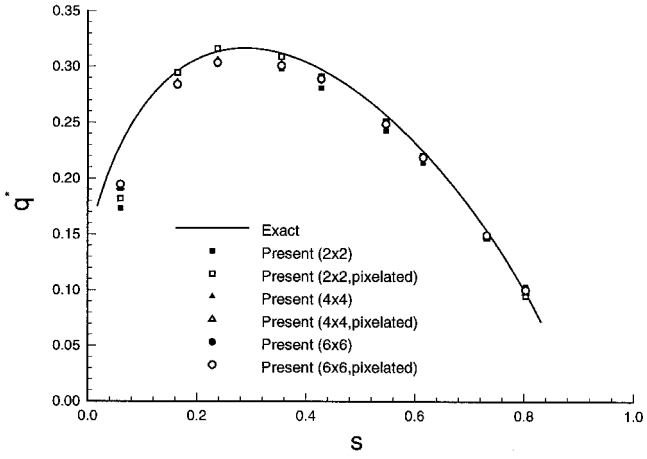

Fig. 11 Tetrahedral enclosure, heat flux variation on face centerline for coarse mesh.

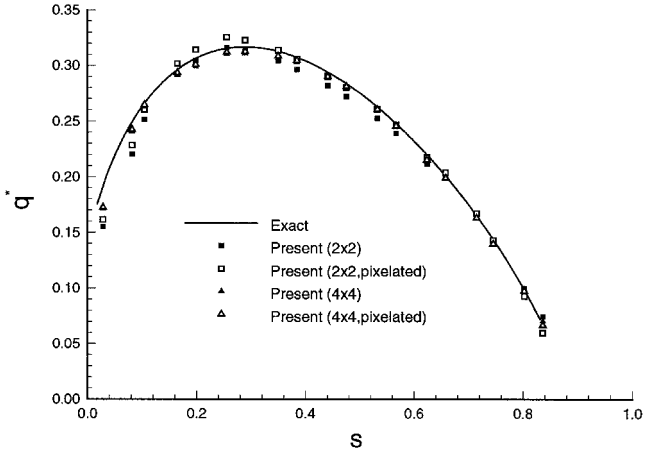

Fig. 12 Tetrahedral enclosure, heat flux variation on face centerline on fine mesh.

coarse mesh are shown in Fig. 11. With approach A, the errors for 2 × 2, 4 × 4, and 6 × 6 angular discretization are 6.8, 4.79, and 4.83%, respectively. With approach B and boundary pixelation, the corresponding errors are 4.08, 4.09, and 4.43%, respectively. The results for the fine mesh are shown in Fig. 12. With approach A, the errors for 2 × 2 and 4 × 4 angular discretization are 4.24 and 2.44%, respectively. With approach B and boundary pixelation, the corresponding errors are 3.27 and 1.81%, respectively.

For the coarse mesh, the error levels are primarily a result of spatial errors. For the finer mesh, pixelation improves accuracy somewhat; however, it does not appear necessary for practical calculations. Calculations using pixelation at interior faces did not change the picture.

The cost of pixelation for the 2 × 2 angular discretization is considered next. Pixelations of 2 × 2, 4 × 4, and 10 × 10 are considered. For coarse mesh the computational time for the pixelated calculations is 2.96, 8.72, and 49.94% greater than that for the unpixelated calculation. For fine mesh the corresponding timings are 1.23, 3.15, and 18.4%.

The coarse tetrahedral mesh has 324 boundary faces and 1946 interior faces, resulting in 0.16 boundary faces per interior face. The fine tetrahedral mesh has 1444 boundary faces and 20,066 interior faces, resulting in 0.07 boundary faces per interior face. The incremental cost of boundary pixelation varies as the ratio of boundary to interior faces. Thus, boundary pixelation is proportionally more expensive on the coarse mesh than on the fine mesh. Most unstructured tetrahedral mesh generators increase the number of interior faces more rapidly than boundary faces as the mesh is refined.

Pixelation is an $\mathbb{O}(n^2)$ process in three dimensions, and its cost escalates rapidly with the degree of pixelation. For all cases studied here, a 4 × 4 pixelation yielded results indistinguishable from a 10 × 10 pixelation, resulting in relatively modest incremental cost.

Radiation in a Purely Scattering Medium

In this problem we consider pure scattering in a square domain. The bottom wall is at T_h. The other walls and the interior are at $T = 0$. We consider the case $\kappa L = 0$, $\sigma_s L = 1.0$. The objective of the computation is to match the net radiative flux on the bottom wall, $q^* = q/(\sigma T_h^4)$, with published results.[14]

An unstructured triangular mesh of 730 cells is used. Computations are done using angular discretizations $N_\theta \times N_\phi$ of 2 × 2, 2 × 4, and 2 × 6, respectively. Only approach A is used in the calculation.

Figure 13 shows a plot of q^* on the bottom wall for all the angular discretizations used. The maximum error in the 2 × 2 angular discretization is 0.75%; the 2 × 4 and the 2 × 6 cases are nearly indistinguishable from each other and have a maximum error of 0.4%.

Coupled Radiation and Natural Convection in a Square Box

Finally, we consider the coupling of buoyancy and participating radiation in a square box. The configuration has been analyzed by Yucel et al.[15] using the S_N discrete ordinates method. The left wall is cold and at T_c. The right wall is hot and at T_h. The top and bottom walls are insulated. Gravity points downward. The enclosure is filled with an absorbing and emitting gas. Computations are done for $Ra = 5 \times 10^6$, $Pr = 0.72$, $T_0/(T_h - T_c) = 1.5$, $\kappa L = 1.0$, and $Pl = k/(4L/\sigma T_0^3) = 0.02$. Here $T_0 = 0.5\ (T_h + T_c)$, and L is the length of the side.

An initial structured quadrilateral mesh of 30 × 30 cells is used with three angular discretizations, 1 × 2, 2 × 4, and 4 × 8. Approach A is used; because the mesh consists of faces aligned with the global angular discretization, control angle overhang does not occur. The fluid flow is computed using

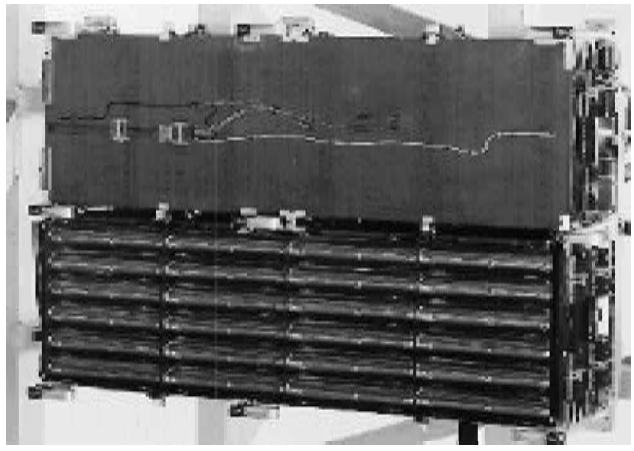

Fig. 13 Pure scattering, radiative heat flux on bottom wall, $\sigma_s L = 1.0$, $\kappa L = 0$.

procedures similar to those described in Mathur and Murthy.[1] A preliminary solution is obtained using a 2×4 angular discretization, and adapted to gradients of temperature using hanging node adaption. The resulting mesh is shown in Fig. 14 and contains 2178 cells. The problem is recomputed on the adapted mesh for all angular discretizations. Figure 15 shows a plot of the normalized u − velocity U $[=uL/(\nu Gr^{1/2})]$ along the vertical centerline of the cavity for all three angular discretizations. Figure 16 shows a corresponding plot of the normalized v − velocity V $[=vL/(\nu Gr^{1/2})]$ along the horizontal centerline. Also plotted are the results of Yucel et al.,[15] obtained using the S_4 approximation (a total of 12 directions).

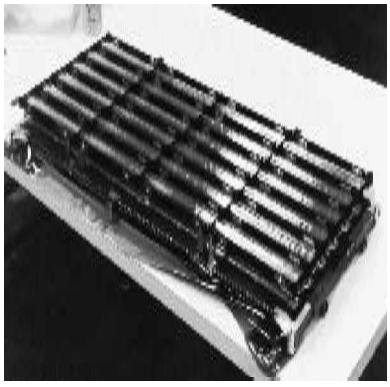

Fig. 14 Coupled convection and radiation in square box, adapted mesh.

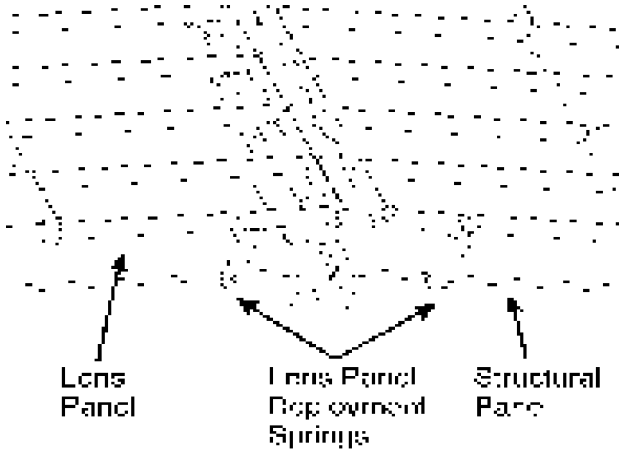

Fig. 15 Coupled convection and radiation in square box, *U*-velocity along vertical centerline.

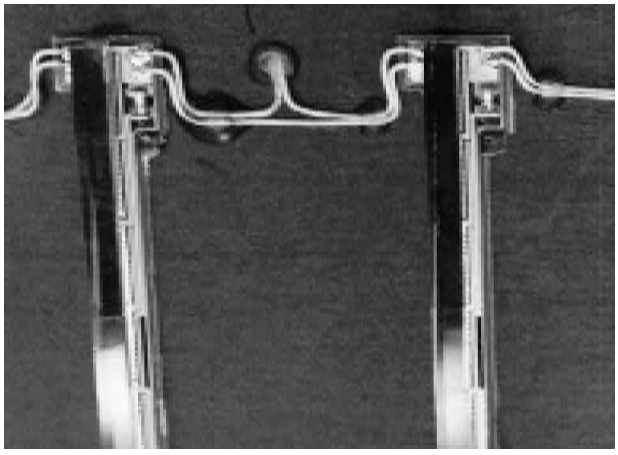

Fig. 16 Coupled convection and radiation in square box, *V*-velocity along horizontal centerline.

Table 2 Coupled convection and radiation in square box[a]

Case	Present	Yucel et al.[15]	% Difference
Nonradiating Nu	14.04	13.82	1.6
Radiating Nu_r			
1×2	31.77	31.77	0.0
2×4	31.58	——	0.6
4×8	31.91	——	0.4
Radiating Nu_t			
1×2	39.42	39.09	0.8
2×4	39.23	——	0.4
4×8	39.61	——	1.3

[a]Nusselt number on hot wall.

The comparison in all cases is good; the three angular discretizations differ from each other by less than 1%. Yucel et al. also reported the hot-wall Nusselt number Nu $\{=q/[k(T_h - T_c)/L]\}$, where q is the hot-wall heat flux. Table 2 reports Nu for both the nonradiating and the radiating case. The nonradiating case is computed on the baseline unadapted mesh. For the radiating case, both the radiation Nusselt number Nu_r and the total Nusselt number Nu_t are reported. The comparison in both cases is good.

Conclusions

The finite volume method for computing radiative heat transfer in absorbing, emitting, and scattering media has been extended to unstructured meshes. The spatial discretization admits arbitrary unstructured convex polyhedra. The procedures for solving directional intensities closely parallel procedures for computing fluid flow. Procedures for the treatment of control angle overhang both at interiors and at boundaries are evaluated. For the problems considered here, accounting for control angle overhang at interior faces appears unnecessary. It is moderately helpful in improving accuracy for coarse angular discretizations if used at boundaries, and incurs only a modest expense. Nevertheless, for many practical problems, the simpler approach A will suffice. The pixelation idea may be used to address control angle overhang caused by reflection and refraction, as well as arbitrary rotational periodicity; here the correct representation of ray rotation is likely to be important. Extensions of the method to these applications are underway and will be reported in due course.

Acknowledgment

We wish to acknowledge the use of Fluent Inc.'s solver, FLUENT/UNS, and its mesh generators, PreBFC and TGrid, in this work.

References

[1]Mathur, S., and Murthy, J., "A Pressure Based Method for Unstructured Meshes," *Numerical Heat Transfer*, Pt. B, Vol. 31, No. 2, 1997, pp. 195–216.

[2]Jiang, Y., and Przekwas, A., "Implicit, Pressure-Based Incompressible Navier-Stokes Equations Solver for Unstructured Meshes," AIAA Paper 94-0305, Jan. 1994.

[3]Demirdzic, I., and Muzaferija, S., "Numerical Method for Coupled Fluid Flow, Heat Transfer and Stress Analysis Using Unstructured Moving Meshes with Cells of Arbitrary Topology," *Comp. Meth. Appl. Mech. Eng.*, Vol. 125, Sept. 1995, pp. 235–255.

[4]Howell, J. R., "Thermal Radiation in Participating Media: The Past, the Present and Some Possible Futures," *Journal of Heat Transfer*, Vol. 110, No. 4(B), 1988, pp. 1220–1226.

[5]Modest, M. F., "Radiative Heat Transfer," *Series in Mechanical Engineering*, McGraw–Hill, New York, 1993.

[6]Menguc, M. P., and Viskanta, R., "Radiative Heat Transfer in Combustion Systems," *Journal of Quantitative Spectroscopy & Radiative Transfer*, Vol. 33, No. 6, 1985, pp. 533–549.

[7]Lockwood, F. C., and Shah, N. P., "A New Radiation Solution Method for Incorporation in General Combustion Prediction Procedures," *Proceedings of the 18th International Symposium on Combustion*, The Combustion Institute, Pittsburgh, PA, 1981, pp. 1405–1414.

[8]Fiveland, W. A., and Jessee, J. P., ''Finite Element Formulation of the Discrete Ordinates Method for Multidimensional Geometries,'' *Journal of Thermophysics and Heat Transfer*, Vol. 8, No. 3, 1994, pp. 426–433.

[9]Raithby, G. D., and Chui, E. H., ''A Finite-Volume Method for Predicting a Radiant Heat Transfer in Enclosures with Participating Media,'' *Journal of Heat Transfer*, Vol. 112, May 1990, pp. 415–423.

[10]Chui, E. H., and Raithby, G. D., ''Computation of Radiant Heat Transfer on a Non-Orthogonal Mesh Using the Finite-Volume Method,'' *Numerical Heat Transfer*, Vol. 23, Pt. B, 1993, pp. 269–288.

[11]Chai, J., Parthasarathy, G., Patankar, S., and Lee, H., ''A Finite-Volume Radiation Heat Transfer Procedure for Irregular Geometries,'' AIAA Paper 94-2095, June 1994.

[12]Chai, J. C., and Moder, J. P., ''Spatial-Multiblock Procedure for Radiation Heat Transfer,'' *HTD-Vol. 332, Proceedings of the ASME Heat Transfer Division*, edited by A. Gopinath, P. D. Jones, J. Syed-Yagoobi, and K. Woodbury, Vol. 1, American Society of Mechanical Engineers, New York, 1996, pp. 119–128.

[13]Hutchinson, B. R., and Raithby, G. D., ''A Multigrid Method Based on the Additive Correction Strategy,'' *Numerical Heat Transfer*, Vol. 9, No. 5, 1986, pp. 511–537.

[14]Chai, J. C., Lee, H. S., and Patankar, S., ''Finite Volume Method for Radiation Heat Transfer,'' *Journal of Thermophysics and Heat Transfer*, Vol. 8, No. 3, 1994, pp. 419–425.

[15]Yucel, A., Acharya, S., and Williams, M. L., ''Natural Convection and Radiation in a Square Enclosure,'' *Numerical Heat Transfer*, Vol. 15, Pt. A, 1989, pp. 261–278.